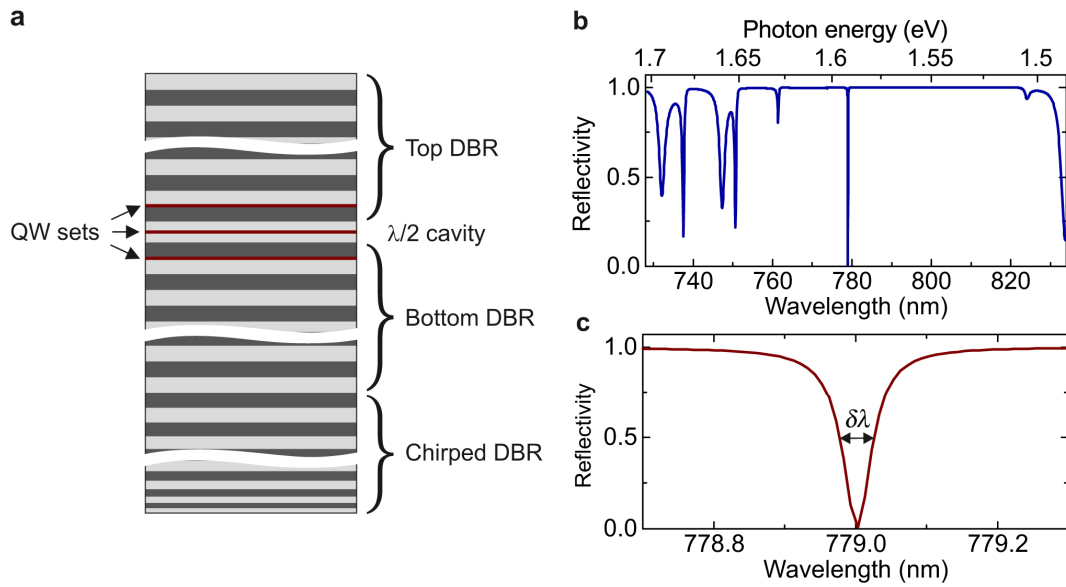
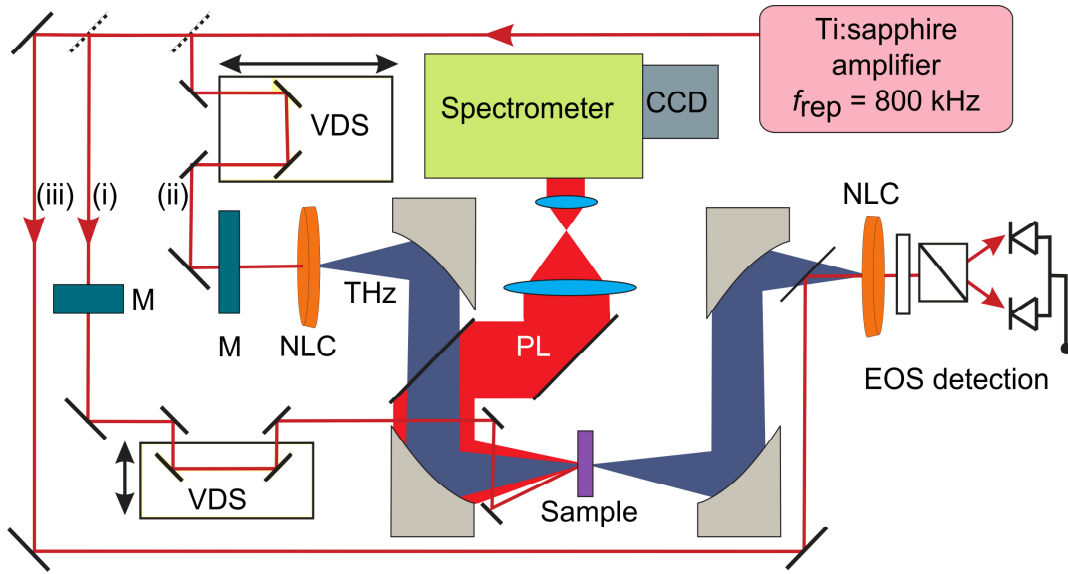


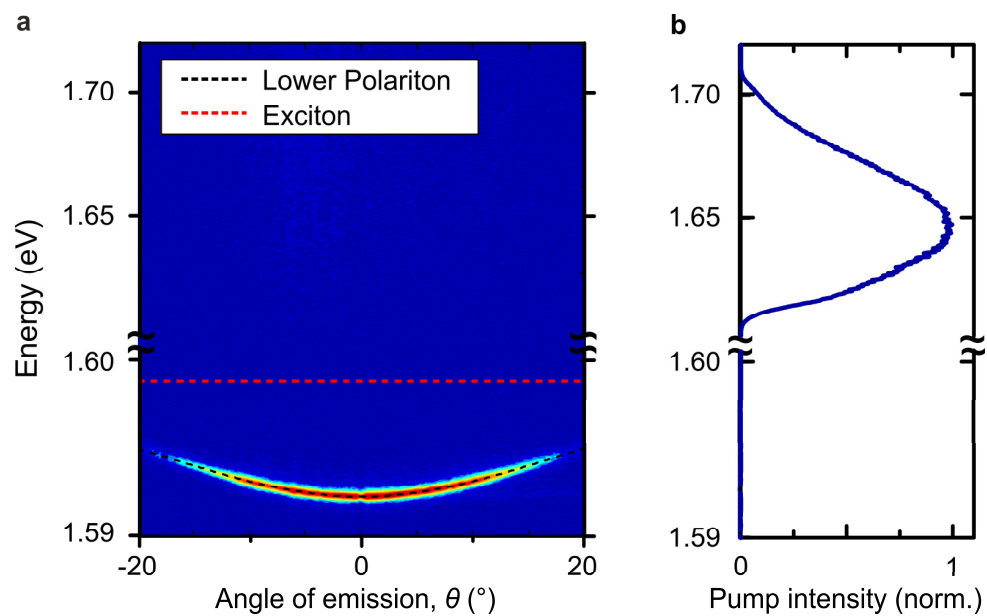
Supplementary Figures



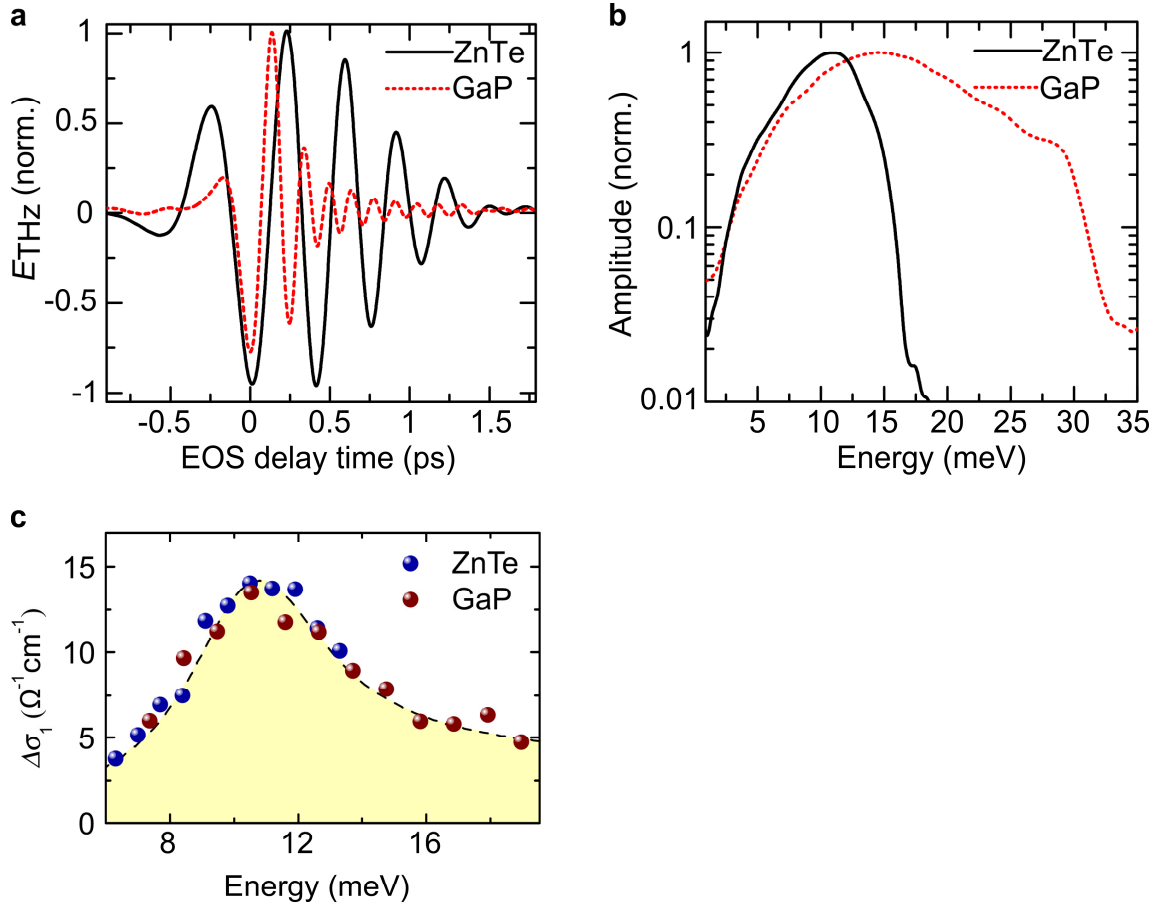
Supplementary Figure 1 | Sample design. **a**, General scheme of the GaAs $\lambda/2$ -cavity including three sets of four GaAs/ $\text{Al}_{0.95}\text{Ga}_{0.05}\text{As}$ quantum wells (QW) (red lines) placed at the centre and the first antinodes of the cavity light field. The microresonator design consists of a top, a bottom and a chirped DBR formed by a stack of 28, 34 and 20 $\text{Al}_{0.2}\text{Ga}_{0.8}\text{As}/\text{AlAs}$ layer pairs, respectively. **b**, Corresponding calculated reflectivity of the microcavity, displayed as a function of wavelength and photon energy. The asymmetry of the high reflectivity window relative to the photonic mode is caused by a 1.5% thickness difference between layers forming the top and bottom DBR. **c**, Close-up view of the calculated reflectivity spectrum in the vicinity of the cavity mode. The linewidth of $\delta\lambda = 0.05$ nm corresponds to a Q-factor of 1.6×10^4 .



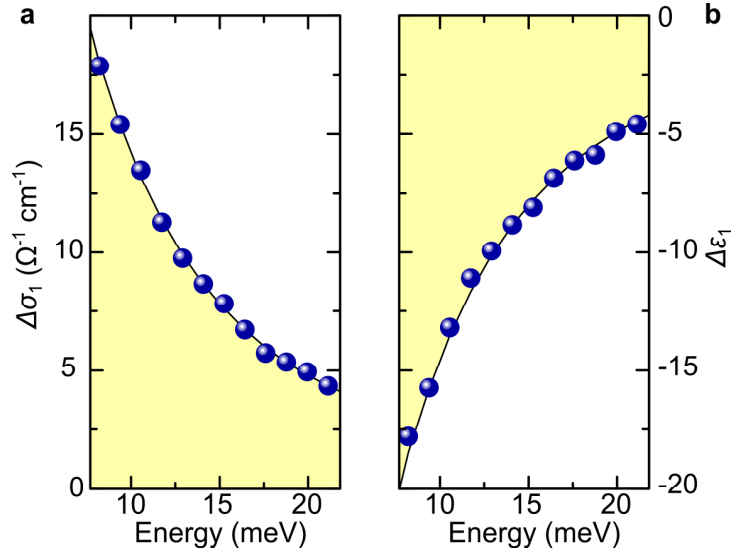
Supplementary Figure 2 | Experimental setup. THz spectroscopy and PL measurements are performed simultaneously. The setup is based on a high-repetition rate femtosecond Ti:sapphire amplifier. f_{rep} : repetition rate, VDS: variable delay stage, NLC: nonlinear optical crystal, EOS: electro-optic sampling, CCD: charge-coupled device (camera), M: optical modulator.



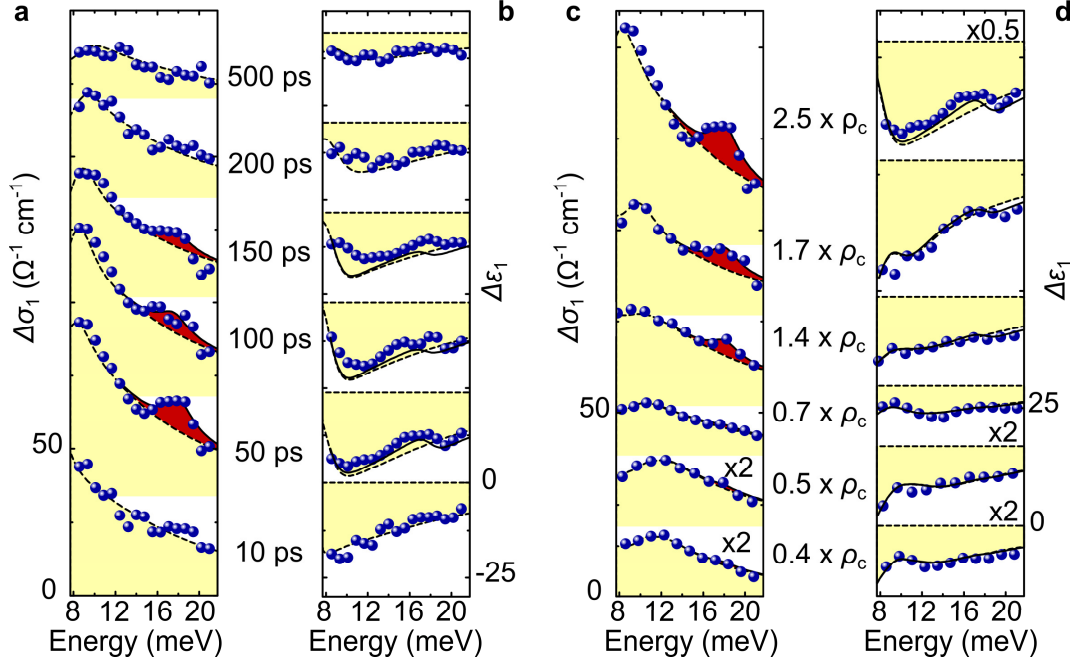
Supplementary Figure 3 | Polaritonic photoluminescence and optical pump spectrum. a, Angle- and energy-resolved PL measurement of the lower polariton with a fitted dispersion on top (black dashed curve). The calculated dispersion relation of the bare exciton is shown as a red dashed line. **b,** Typical pump spectrum with a centre energy of 1.65 eV (FWHM: 0.05 eV) for nonresonant optical injection of unbound electron-hole pairs.



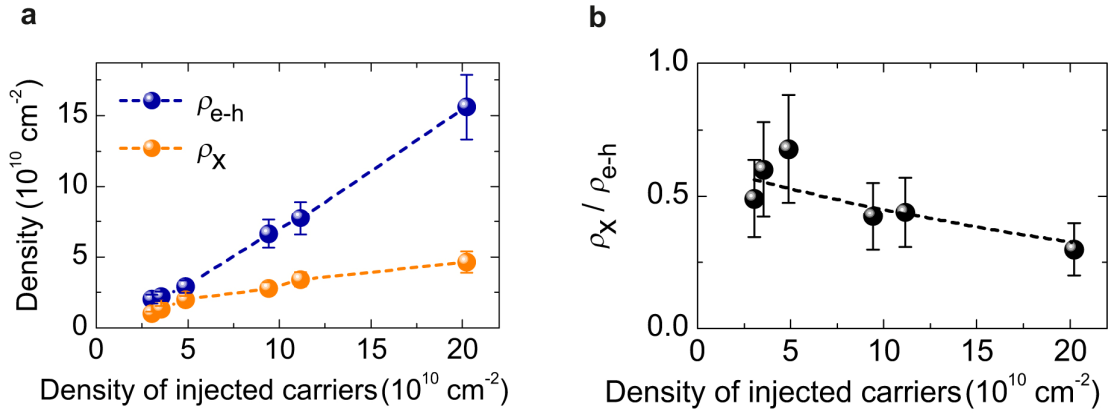
Supplementary Figure 4 | Typical THz probe pulses. **a**, Time-resolved THz signal obtained with a combination of identical (110)-oriented ZnTe emitter and detector crystals of a thickness of 200 μm (solid curve) and (110)-oriented GaP emitter and detector crystals of a thickness of 200 μm (dotted curve). **b**, Corresponding amplitude spectra obtained by Fourier transformation of the time-resolved signal. **c**, Real part of the pump-induced THz conductivity $\Delta\sigma_1$ at $\rho = 0.8 \times \rho_c$ and $\tau = 300$ ps obtained with ZnTe (blue spheres) and GaP (red spheres) emitter and detector crystal pairs. Broken curve: two-component model fitting $\Delta\sigma_1$. The lattice temperature is 10 K.



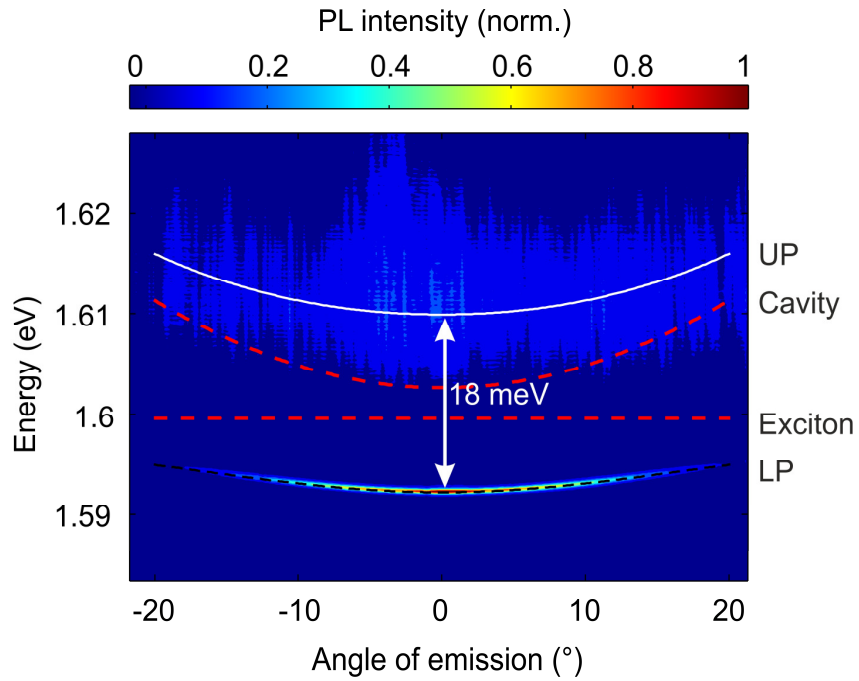
Supplementary Figure 5 | Complex-valued THz response of a plasma of unbound electron-hole pairs. **a**, Real part of the pump-induced THz conductivity $\Delta\sigma_1$ and, **b**, corresponding real part of the dielectric function $\Delta\epsilon_1$ of the microcavity obtained at $T_L = 150$ K and $\tau = 50$ ps. Blue spheres: experiment, black curves: Drude model simultaneously fitting $\Delta\sigma_1$ and $\Delta\epsilon_1$ with the following parameters: carrier density $\rho = 6.1 \times 10^{10} \text{ cm}^{-2}$ and scattering rate $\Gamma_D = 11$ THz.



Supplementary Figure 6 | Full complex-valued THz response of condensed polaritons. **a** and **c** reproduce the real part of the pump-induced THz conductivity $\Delta\sigma_1$ (**a**) as a function of delay time τ , for fixed $\rho = \rho_c$, and (**c**) as a function of excitation density ρ , for fixed $\tau = 50$ ps, as displayed in Figs. 4a and b in the main text. **b** and **d** show the real part of the dielectric function $\Delta\varepsilon_1$ corresponding to both situations. Blue spheres: experimental data, black broken curves: two-component model fitting simultaneously $\Delta\sigma_1$ and $\Delta\varepsilon_1$. The corresponding densities ρ_x and ρ_{e-h} extracted from the fits to **a** are displayed in Fig. 4e of the main text. Red shadows in **a** and **c**: A Lorentz function (FWHM = 3 meV) traces the departures between the experimental data and the two-component model due to polariton population at $k_{\parallel} = 0$. The corresponding dispersive features in the dielectric function are shown as solid curves in **b** and **d**.

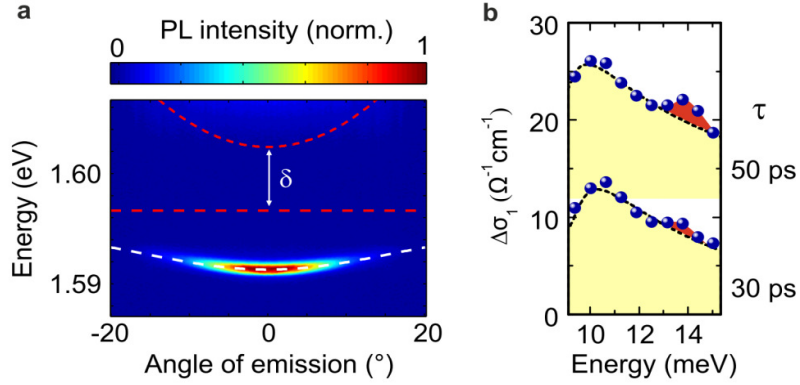


Supplementary Figure 7 | Exciton and free carrier densities. **a**, Densities of free carriers, ρ_{e-h} , (blue spheres) and reservoir excitons, ρ_X , (orange spheres) extracted from the two-component model used to fit the data of Fig. 4b of the main text. The data are displayed as a function of the total injected carrier density ρ and the pump delay time τ is fixed at $\tau = 50$ ps. The dashed lines are guides to the eye. **b**, Ratio ρ_X / ρ_{e-h} of reservoir exciton and free carrier densities calculated from Supplementary Figure 7a. The dashed line is a guide to the eye. The lattice temperature is 10 K.

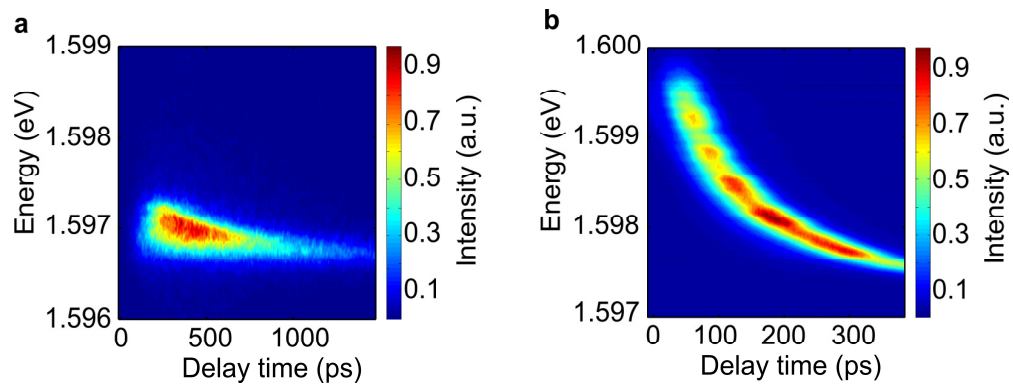


Supplementary Figure 8 | PL measurements showing both UP and LP dispersions.

Angle- and energy-resolved PL measurement associated to the lower (LP) and upper polariton (UP) with fitted dispersions corresponding to the black dashed curve and white plain curve, respectively. The sample is kept at a temperature of 30 K. The calculated dispersion relation of the bare exciton and the bare cavity mode are shown as red dashed lines. The energy separation between the lower and the upper polariton at $k_{\parallel} = 0$, associated to the vacuum Rabi splitting, is 18 meV.



Supplementary Figure 9 | PL and THz response of condensed polaritons from a microcavity with $\delta = 6$ meV. **a**, Angle-resolved PL spectra ($\rho = 0.2 \times \rho_c$) and numerical fit of the dispersion of the LP branch (broken white line) assuming positive detuning $\delta = 6 \pm 1$ meV. **b**, Real part of the pump-induced THz conductivity $\Delta\sigma_1$ for different delay times τ (indicated next to the curves) after photoinjection of unbound electron-hole pairs of a density $\rho = 1.4 \times \rho_c$. Blue spheres: experimental data, black curves: two-component model fitting $\Delta\sigma_1$ and $\Delta\varepsilon_1$. Emitters and detectors: 200- μm -thick ZnTe crystals. The sample is kept at a temperature of 10 K. The characteristic polaritonic 1s-2p resonance (highlighted by the red area) tracing the matter part of the condensate is positioned at $\hbar\omega = 14$ meV.



Supplementary Figure 10 | Time-resolved PL intensity. **a** and **b**, Spectrally and temporally resolved PL intensity at excitation densities of $\rho_1 < \rho_c$ (**a**) and $\rho_2 > \rho_c$ (**b**). Spectral integration of these data sets leads to the PL curves shown in Figs. 4d and e, respectively.

Supplementary Discussion

Transition energy between LP at $k_{\parallel} = 0$ and 2p excitonic state. The THz response observed above the threshold fluence (Fig. 4) shows a clear emerging feature at $\hbar\omega = 17$ meV corresponding to the transition between the polariton condensate at $k_{\parallel} = 0$ and the optically dark 2p excitonic state. With two independent measurements, we confirm that the observed transition energy corresponds to the sum of the 1s-2p transition energy of the bare excitons and the energy spacing between the condensate and the undressed 1s excitonic state as depicted in Fig. 1. First, THz measurements performed at early time delays ($\tau < 50$ ps) show a 1s-2p transition energy of $\hbar\omega = 9$ meV before polaritons redistribute towards lower energy states of the LP branch. This value is consistent with previous reports on the binding energy of bare excitons in 7-nm-thick GaAs QWs¹⁻³. The energy shift of the 1s state induced by strong light-matter coupling can be independently inferred from an angle-resolved PL measurement tracing both the UP and LP dispersions. Nonresonant carrier injection allows us to observe PL originating from the LP only. PL associated to a polariton population occupying the UP branch could not be detected since the quasi-particles quickly relax down in energy to the LP branch via carrier-carrier or carrier-phonon scattering processes. To resolve simultaneously the dispersion of both UP and LP branches, we inject carriers resonantly in the UP level and keep the sample at an elevated temperature of 30 K (see Supplementary Figure 8). The broader emission of the UP branch in photon energy attests to the shorter lifetime of the upper polaritons. A numerical fit based on the theoretical polariton dispersion⁴ allows us to determine the energy separation between the lowest state of the LP branch at $k_{\parallel} = 0$ and the undressed 1s excitonic state to amount to 8 meV. Hence the complete energy spacing between the dressed 1s and the dark 2p state is anticipated at 17 meV confirming the experimental observation of the corresponding THz absorption maximum in Fig. 4. The numerical fit of the polariton dispersion of Supplementary Figure 8 also yields a vacuum Rabi energy of 18 meV, which is 20% higher than the value achieved in standard microcavity design. This increased vacuum Rabi energy agrees with transfer matrix calculations^{5,6} showing a corresponding enhancement of the coupling strength between excitons and the photonic mode in our structure caused by the chirped DBR.

The intra-polaritonic absorption at $k_{\parallel} = 0$ is expected to shift as a function of the cavity detuning δ . In PL experiments δ is readily shifted in wedge-shaped cavities exhibiting different effective cavity lengths for different locations on the sample. In our THz

experiments the large diffraction-limited THz probe spot sets more stringent boundaries. In order to keep a homogeneous cavity length over the entire THz probe spot, our microcavities have to be exceptionally plane parallel. In order to vary δ , we thus need to prepare a separate set of samples optimized for various values of the detuning. As a first example, Supplementary Figure 9 presents PL and THz data collected from a sample with $\delta = 6 \pm 1$ meV.

This detuning differs significantly from the value implemented in the main text ($\delta = 2$ meV). The angle-resolved PL data (Supplementary Figure 9a) allow us to confirm the absolute value of δ by fitting the dispersion of the lower polariton branch. Note that the 1 meV uncertainty for δ is due to a relatively large detuning gradient (0.5 meV/mm) of that particular sample. Larger δ leads to a reduced energy spacing of 6 meV between the polariton condensate and the bare 1s excitonic state. Correspondingly, the intra-excitonic 1s-2p transition at $k_{\parallel} = 0$ is expected to occur at an approximate photon energy of 14 meV. The real part of the optical conductivity measured above threshold ($\rho = 1.4 \times \rho_c$) for $\tau = 30$ and 50 ps (Supplementary Figure 9b) does indeed contain this characteristic peak at $\hbar\omega = 14$ meV while the dominant maximum at $\hbar\omega = 9$ meV is again associated to the 1s-2p transition of bare excitons in the reservoir.

Exciton vs. free carrier densities. In our experiments, the maximum carrier density injected in the microcavity QWs is ultimately limited by the output power of our optical source. Although the present study focuses on the polariton lasing regime and the dynamics leading to it, an analysis of the THz response with increasing pump fluence sheds light onto the question of how the polariton lasing regime may ultimately cross over into the photon lasing regime observed at extremely high pump fluences⁷⁻¹⁰.

From the parameters extracted from the fitting model, one can analyse the ratio between exciton and free carrier densities as the excitation pump fluence is increased. Supplementary Figures 7a and b show these densities and their ratio retrieved from THz measurements performed at a fixed time delay of 50 ps between the NIR pump and the THz probe pulse. The analysis confirms that for all accessible fluences there is always a considerable share of excitons. Yet the fraction of bound to unbound electron-hole pairs decreases with increasing pump fluences. It will be interesting in future studies to track this feature for yet higher pump pulse energies approaching the threshold for conventional photon lasing. The current data

suggest a smooth onset of a density driven Mott transition towards a regime dominated by free carriers as reported previously for bare QWs¹¹.

Time-resolved photoluminescence measurements. Using a streak camera, we resolve the PL intensity with respect to photon energy and delay time, for different excitation densities ρ . Supplementary Figures 10a and b show the results for $\rho = \rho_1 < \rho_c$ and $\rho_2 > \rho_c$, respectively. Below threshold, strong PL sets in with a distinct time delay of 200 ps after photoexcitation of free carriers, while the broad emission spectrum undergoes a negligible redshift of less than 0.5 meV with time. This behaviour is consistent with the formation of excitons and subsequent cooling towards the lower polariton branch, occupying a broad range of in-plane momenta k_{\parallel} . Since the lower polariton ensemble is constantly fed by the reservoir of large-momentum excitons, the decay of the PL signal is expected to be determined by the exciton lifetime. The observed value of 1 ns is consistent with this picture. In sharp contrast, the PL intensity sets on substantially faster for $\rho_2 > \rho_c$ (Supplementary Figure 10b). The central photon energy starts out with a blueshift of about 2 meV, larger than the one observed for $\rho_1 < \rho_c$. The energy then continuously relaxes back to its low-density value. This dynamics is expected in the case of polariton condensation, where bosonic stimulation leads to a rapid occupation of the metastable lower polariton branch at $k_{\parallel} = 0$ and polariton repulsion causes a slight blueshift of the PL signature^{4,12,13}. Spectral integration of the two-dimensional maps of Supplementary Figure 10 results in the temporal evolution of the PL intensity shown in Figs. 4d and e of the main text. Note that a transition from polariton lasing to ordinary photon lasing in the regime of weak light-matter coupling would manifest itself as a characteristic discontinuous jump of the central photon energy with increasing pump fluence. Such a feature is not observed in our data as long as the pump fluence remains below a value of $\Phi = 200 \mu\text{J}/\text{cm}^2$, which corresponds to an excitation density of roughly $\rho = 6 \times \rho_2$.

Supplementary Methods

Microcavity design. Custom-tailored semiconductor microcavities are the key to all of our experiments. We use an AlAs $\lambda/2$ cavity which is contained within two planar distributed Bragg reflectors (DBRs) made of $\text{Al}_{0.2}\text{Ga}_{0.8}\text{As}/\text{AlAs}$ layer pairs, as shown in Supplementary Figure 1a. Top and bottom DBRs contain, respectively, 28 and 34 pairs. Three series of 4 quantum wells (QWs) are inserted at the centre and the first antinodes of the cavity. The 7-nm-thick QWs are separated by 3-nm-thick AlAs barrier layers. At a temperature of 10 K, the photonic mode of the microcavity is strongly coupled to the heavy hole 1s-exciton interband transition of the quantum wells, with a vacuum Rabi splitting¹⁴ of 18 meV and a detuning δ of 2 meV. Although the general epitaxial layout is based on structures used in previously reported experiments on polariton condensation, we made two major adjustments to the sample design to maximize the efficiency of nonresonant carrier injection with our Ti:sapphire ultrafast optical source. First, the relative thickness of top and bottom DBR layers is engineered to shift the first high-energy reflectivity minimum of the cavity towards the centre wavelength of our optical source at 750 nm (Supplementary Figure 1b). Then, at the back of the sample, an additional chirped DBR is used to increase the spatial overlap between the QWs and the excitation wave. This chirped DBR is made of 20 $\text{Al}_{0.2}\text{Ga}_{0.8}\text{As}/\text{AlAs}$ layer pairs of gradually decreasing thickness and it is designed to efficiently reflect the excitation pulse spectrum. Although, our sample design differs notably from standard microcavities, the cavity's Q-factor is expected at 1.6×10^4 , corresponding to a theoretical linewidth of $\delta\lambda = 0.05$ nm (Supplementary Figure 1c). PL measurements at low excitation fluence (e.g. Supplementary Figure 10a) allow us to confirm a Q-factor larger than 6000, limited by the setup's spectral resolution. Finally, the GaAs substrate on which the heterostructure is grown is removed and the microcavity is placed on a diamond window ensuring optimal THz transmissivity over all photon energies used in our experiment. More details on this special sample design will be presented in a future publication.

Microcavity samples used in standard PL experiments are usually designed with a wedge-shaped cavity featuring different resonance frequencies at different locations on the sample. This allows for an easy adaption and variation of δ by lateral displacement of the structure with respect to the pump and probe beam. For THz probing this strategy is obstructed by diffraction: The large diffraction-limited THz probe spots (FWHM diameter: ~ 0.3 mm)

require specifically plane parallel Bragg mirrors. Our samples achieved a δ gradient smaller than 0.3 meV over 1 mm displacement ensuring a homogeneous probing with the THz pulse.

Experimental setup. The experimental setup tracing, simultaneously, angle-resolved photoluminescence (PL) spectra and time-resolved terahertz (THz) absorption of condensing exciton polaritons is shown in Supplementary Figure 2. The system is based on a Ti:sapphire amplifier generating tuneable femtosecond pulses at a repetition rate of 800 kHz¹⁵. For the experiments discussed here, the centre wavelength is set to 750 nm (photon energy: 1.65 eV, pulse duration: 20 fs) and the pulse train is split into three optical branches. Pulses in branch (i) nonresonantly inject free carriers into the QWs. THz probe transients are generated by optical rectification (OR) of laser pulses in branch (ii) and get focussed onto the microcavity. In the sample, the pump beam diameter exceeds the THz FWHM by a factor of 2 in order to ensure the probing of a homogenous carrier density. Finally, pulses in branch (iii) serve as optical gates for electro-optic sampling (EOS) of the THz pulses transmitted through the microcavity. Using dual lock-in detection, the sensitivity of EOS routinely reaches the shot-noise limit of the gate pulses. We record simultaneously the THz transient transmitted through the unexcited sample and the pump-induced changes of the THz field. From this data set, we obtain the frequency dependent changes of the instantaneous complex-valued field transmission $\Delta T(\omega)$ caused by photoexcitation. A translation stage in branch (ii) varies the delay time τ between the maximum of the pump pulse and the THz probe to study the dynamics of the system. Simultaneously, the PL intensity is collected from the front side of the microcavity via the parabolic mirror that also focuses the THz pulses onto the sample. A silicon wafer, transparent to THz radiation, separates the PL light by reflecting it towards a spectrometer. The Fourier plane of the parabolic mirror is projected onto the vertical slit of a monochromator equipped with a charge-coupled device (CCD) camera. This setup allows us to resolve the PL distribution with respect to energy and the angle of emission, which is associated to the photon in-plane momentum, k_{\parallel} .

Nonresonant injection of unbound electron-hole pairs. Efficient injection of unbound electron-hole pairs is achieved by optimizing the spectral overlap between the pump pulse and the reflectivity minima of the microcavity sample located above the stop band, at $\hbar\omega_p = 1.65$ eV. Supplementary Figure 3a shows an angle- and energy-resolved PL measurement with theoretical fits based on the dispersion of the LPB (black dashed curve)

and the bare 1s-excitonic level (red dashed line)⁴. The optical pump spectrum used for nonresonant carrier injection into the QWs is depicted in Supplementary Figure 3b on the same energy scale. Densities of photoinjected electron-hole pairs are determined independently via careful measurements of the absorbed pump fluences and via direct analysis of the THz response. The values obtained in both ways agree well within an error margin of 20%.

Generation and detection of THz radiation. The THz field transients are generated by OR in a nonlinear optical crystal. The electromagnetic waveforms are time-resolved by EOS with a second identical crystal. In our experiment, two different pairs of emitters and detectors were available to optimize the sensitivity for selected spectral regions. To resolve weak pump-induced changes induced by a carrier density $\rho < \rho_c$, we use a pair of 200- μm -thick, (110)-oriented ZnTe crystals that provide an optimal resolution in the low photon energy range ($6 \text{ meV} < \hbar\omega < 14 \text{ meV}$). Population build-up in the reservoir can then be traced accurately as it displays a characteristic THz absorption maximum around $\hbar\omega = 9 \text{ meV}$ (see Fig. 3). For measurements at $\rho > \rho_c$, enhanced pump-induced signal levels allow us to use a pair of 200- μm -thick, (110)-oriented GaP crystals, instead. Although the sensitivity of this emitter-detector combination is reduced by a factor of ~ 5 at $\hbar\omega = 9 \text{ meV}$ in comparison to the ZnTe configuration, the larger signal obtained at high ρ compensates for the loss of THz probe sensitivity. More importantly, phase-matching in GaP provides access to a broader THz spectrum ($8 \text{ meV} < \hbar\omega < 22 \text{ meV}$) which is used to cover all intra-polaritonic transitions including the 1s-2p resonance associated to the matter part of the polariton condensate at $\hbar\omega = 17 \text{ meV}$. Supplementary Figures 4a and b show THz waveforms obtained for both crystal combinations, along with their respective amplitude spectra. In Supplementary Figure 4c, a direct comparison of THz measurements of $\Delta\sigma_1$ obtained with both crystal pairs at a transient density of $\rho = 0.8 \times \rho_c$ confirms the consistency between the data sets presented in Figs. 3 and 4.

Complex dielectric function. The optical pump injects carriers in the QWs embedded within the microcavity and induces an amplitude and phase change in the transmitted THz transient. The pump-induced transmission change $\Delta T(\omega)$ is caused by a frequency dependent variation of the complex dielectric function of the QWs, $\Delta\epsilon(\omega) = \Delta\epsilon_1(\omega) + i\Delta\epsilon_2(\omega)$, where

$\Delta\varepsilon_2(\omega) = \Delta\sigma_1(\omega)/(\omega\varepsilon_0)$, and ε_0 is the vacuum permittivity. The exact value for $\Delta\varepsilon(\omega)$ can be retrieved numerically from the experimental function $\Delta T(\omega)$ by means of a transfer matrix formalism^{5,6,11}. This approach takes into account the full structure design of the microcavity and the linear dielectric functions of the different $\text{Al}_x\text{Ga}_{1-x}\text{As}$ compounds^{16,17} and yields $\Delta\varepsilon_1(\omega)$ and $\Delta\sigma_1(\omega)$ as displayed in Figs. 3, 4 and Supplementary Figures 5 and 6.

To demonstrate the consistency of our formalism, we collect THz transmission data of the microcavity at $T_L \geq 150$ K where the thermal energy exceeds the exciton binding energy and the free carrier contribution is expected to dominate the THz response. Typical experimental values for $\Delta\sigma_1$ and $\Delta\varepsilon_1$ are shown in Supplementary Figures 5a and b. The data follow closely a straightforward Drude response (solid curves) clearly proving the validity of our transfer matrix formalism. Since ordinary photon lasing in semiconductor devices occurs due to interband recombination of unbound electron-hole pairs – in the absence of excitons and strong light-matter coupling – the above Drude-like THz polarization is also expected to prevail in conventional photon lasers.

Figure 3 of the main text displays the full complex-valued dielectric function of the microcavity for the example of low excitation densities. Analogously the complete response function is retrieved also for all other excitation densities. For brevity reasons, however, Fig. 4 concentrates only on $\Delta\sigma_1(\omega)$. Supplementary Figure 6 summarizes the full data set, including $\Delta\sigma_1(\omega)$ and $\Delta\varepsilon_1(\omega)$, as a function of the delay time τ and the excitation density ρ , respectively.

We start by discussing the dynamics of the THz response for a high excitation density $\rho = \rho_2 > \rho_c$ (Supplementary Figures 6a and b). The pump pulse injects unbound electron-hole pairs above the band gap. Accordingly, the spectra of both $\Delta\sigma_1$ and $\Delta\varepsilon_1$ obtained immediately after the pump pulse are well reproduced by the Drude model. Already 50 ps later, however, a conductivity maximum centred at a photon energy of 9 meV indicates the formation of excitons in the reservoir. Consistently, this dynamics is also reflected in the dielectric function, where a steep negative slope due to the characteristic dispersive profile of a resonance occurs. The availability of both response functions, $\Delta\sigma_1$ and $\Delta\varepsilon_1$, poses strict boundaries for any theoretical model. As a first approximation, we adapt a phenomenological two-component model simultaneously to both $\Delta\sigma_1$ and $\Delta\varepsilon_1$ (broken curves). While the numerical fits achieve satisfactory agreement with the experimental data for most photon energies, delay times and excitation densities, polariton condensation causes striking deviations from the simplistic model (see red shadows in Supplementary Figure 6a).

Importantly the characteristic maxima of $\Delta\sigma_1(\omega)$ centred at a photon energy of 17 meV are clearly associated with a dispersive feature in $\Delta\varepsilon_1(\omega)$ (Supplementary Figure 6b), confirming the new 1s-2p resonance caused by a macroscopic population of polaritons at $k_{\parallel}=0$. Analogously the correlated emergence of a maximum of the conductivity and a dispersive feature of the dielectric function is also observed as a function of the excitation density ρ (Supplementary Figures 6c and d, respectively).

Theoretical model and fitting parameters. Our experimental data shown in Figs. 3 and 4 are fitted using a phenomenological two-component model that includes the simultaneous contributions of excitons and unbound electron-hole pairs, with respective densities ρ_X and ρ_{e-h} . Within this approximation pump-induced changes in the complex dielectric function are expressed as follows¹⁸:

$$\Delta\varepsilon(\omega) = \rho_X\Delta\varepsilon_X(\omega) + \rho_{e-h}\Delta\varepsilon_D(\omega) \quad (1)$$

where $\Delta\varepsilon_X(\omega)$ accounts for the change in the dielectric function due to internal resonances of bare excitons and $\Delta\varepsilon_D(\omega)$ is the Drude response. These two frequency dependent functions are described in detail in Ref. 18. The dynamics of ρ_X and ρ_{e-h} are displayed in Fig. 4 of the main text for injected carrier densities $\rho_1 < \rho_c$ and $\rho_2 > \rho_c$. The experimental shift of the THz feature associated to the 1s-2p transition could only be reproduced by variation of the 1s-2p energy spacing, as discussed in the main text. Remaining fit parameters of the model include the Drude scattering rate Γ_D of free carriers as well as the widths of the excitonic transitions between two bound states Γ_{BB} and transitions from bound states to the continuum Γ_{BC} , which were kept nearly constant for both excitation densities. As a result, we can confidently attribute the paramount changes observed in the THz dynamics to the variations in ρ_X and ρ_{e-h} . Since the phenomenological model is bound to simultaneously reproduce both real and imaginary parts of $\Delta\varepsilon$ over a broad frequency range, the extracted quantities are reliable and reproducible. It will be interesting to compare the retrieved values with the ones extracted from fully quantum mechanical models of the THz exciton and free carrier response¹⁹.

Supplementary References

1. Bastard, G., Mendez, E. E., Chang, L. L. & Esaki, L. Exciton binding energy in quantum wells. *Phys. Rev. B* **26**, 1974–1979 (1982).
2. Gurioli, M. *et al.* Well-width and aluminum-concentration dependence of the exciton binding energies in GaAs/Al_xGa_{1-x}As quantum wells. *Phys. Rev. B* **47**, 15755 (1993).
3. Oelgart, G. *et al.* Experimental and theoretical study of excitonic transition energies in GaAs/Al_xGa_{1-x}As quantum wells. *Phys. Rev. B* **49**, 10456 (1994).
4. Kavokin, A., Baumberg, J. J., Malpuech, G. & Laussy, F. P. *Microcavities* (Oxford University Press: Oxford, NY, USA, 2007).
5. Ulbricht, R., Hendry, E., Shan, J., Heinz, T. F. & Bonn, M. Carrier dynamics in semiconductors studied with time-resolved terahertz spectroscopy. *Rev. Mod. Phys.* **83**, 543–586 (2011).
6. Furman, S. & Tikhonravov, A. V. *Basics of optics of multilayer systems*. (Edition Frontières: Singapore, 1992).
7. Deng, H., Weihs, G., Snoke, D., Bloch, J. & Yamamoto, Y. Polariton lasing vs. photon lasing in a semiconductor microcavity. *Proc. Natl. Acad. Sci.* **100**, 15318–15323 (2003).
8. Kasprzak, J., Solnyshkov, D. D., André, R., Le Si Dang & Malpuech, G. Formation of an exciton polariton condensate: thermodynamic versus kinetic regimes. *Phys. Rev. Lett.* **101**, 146404 (2008).
9. Tempel, J.-S. *et al.* Characterization of two-threshold behavior of the emission from a GaAs microcavity. *Phys. Rev. B* **85**, 075318 (2012).
10. Tsotsis, P. *et al.* Lasing threshold doubling at the crossover from strong to weak coupling regime in GaAs microcavity. *New J. Phys.* **14**, 023060 (2012).
11. Huber, R., Kaindl, R. A., Schmid, B. A. & Chemla, D. S. Broadband terahertz study of excitonic resonances in the high-density regime in GaAs/Al_xGa_(1-x)As quantum wells. *Phys. Rev. B* **72**, 161314 (2005).
12. Kasprzak J. *et al.* Bose-Einstein condensation of exciton polaritons. *Nature* **443**, 409–414 (2006).
13. Wertz, E. *et al.* Spontaneous formation and optical manipulation of extended polariton condensates. *Nature Phys.* **6**, 860–865 (2010).
14. Weisbuch, C., Nishioka, M., Ishikawa, A. & Arakawa, Y. Observation of the coupled exciton-photon mode splitting in a semiconductor quantum microcavity. *Phys. Rev. Lett.* **69**, 3314–3317 (1992).

15. Huber, R. *et al.* 12-fs pulses from a continuous-wave-pumped 200-nJ Ti:sapphire amplifier at a variable repetition rate as high as 4 MHz. *Opt. Lett.* **28**, 2118–2120 (2003).
16. Palik, E. D. Handbook of Optical Constants of Solids I. (Academic: Orlando, 1985).
17. Palik, E. D. Handbook of Optical Constants of Solids II. (Academic: San Diego, 1991).
18. Kaindl, R. A., Hägele, D., Carnahan, M. A. & Chemla, D. S. Transient terahertz spectroscopy of excitons and unbound carriers in quasi-two-dimensional electron-hole gases. *Phys. Rev. B* **79**, 045320 (2009).
19. Haug, H. & Koch, S. W. Quantum Theory of the Optical and Electronic Properties of Semiconductors (5th ed.). (World Scientific: Singapore, 2009).